# Development of a single-cell x-ray fluorescence flow cytometer

Authors

**Andrew M. Crawford[a], Patrick Kurecka[a], Tsz Kwan Yim[a], Claire Kozemchak[a], Aniruddha Deb[ab], Lubos Dostal[a], Cheng-Jun Sun[c], Dale L. Brewe[c], Raul Barrea[d] and James E. Penner-Hahn[ab]***

[a]Department of Chemistry, University of Michigan, Ann Arbor, MI, 48109-1055, USA
[b]Department of Biophysics, University of Michigan, Ann Arbor, MI, 48109-1055, USA
[c]X-ray Science Division, Argonne National Laboratory, 9700 Cass Avenue, Argonne, IL, 60439, USA
[d]Department of Physics, DePaul University, Chicago, IL, 60604, USA

Correspondence email: jeph@umich.edu

**Synopsis** We describe and develop an x-ray fluorescence flow cytometer capable of performing single cell metal analysis. This device is capable of detecting µM concentrations from fL sample volumes.

**Abstract** We have developed an x-ray fluorescence flow cytometer that can determine the total metal content of single cells. Capillary action or pressure were used to load cells into hydrophilic or hydrophobic capillaries, respectively. Once loaded, the cells were transported at a fixed vertical velocity past a focused x-ray beam. X-ray fluorescence was then used to determine the mass of metal in each cell. By making single-cell measurements we can directly measure population heterogeneity for metals in the µM to mM concentration range on fL sample volumes, a measurement that is difficult using most analytical methods. We have used this approach to determine the metal composition of 936 individual bovine red blood cells (bRBC), 31 individual 3T3 mouse fibroblasts (NIH3T3), and 18 *Saccharomyces cerevisiae* (yeast) cells with an average measurement frequency of ~ 4 cells/minute. These data show evidence for surprisingly broad metal distributions. Details of the device design, data analysis, and opportunities for further sensitivity improvement are described.

**Keywords: flow cytometry, x-ray fluorescence, single cell, metallome, homeostasis**

## 1. Introduction

In addition to their organic constituents, cells contain a variety of bulk, trace and ultra-trace elements. In most cases, cells appear to have homeostatic mechanisms that maintain elemental concentrations within narrow limits. Knowledge of these cellular concentrations under different conditions is important for understanding homeostasis. Relevant concentrations range from ~10 – 100 mM for bulk elements (*e.g.*, P, K, Na, and Fe in red blood cells) to 0.1 – 3 mM for trace elements (*e.g.*, Zn, Mg, Ca, and Fe in other cell types) to 1 – 20 µM for ultra-trace elements (Cu, Ni, Mn, Se) (Herring *et* *al.*, 1960a, Shamberger, 2003). These concentrations are perturbed under various conditions and disease states (Herring *et al.*, 1960b, Kakkar & Makkar, 2009), and these variations can be clinically diagnostic. For example, patients with spherocytosis have red blood cells with higher than normal Fe content in relation to their volume (Kakkar & Makkar, 2009).

Toxic metals can also result in disruption of metal concentrations. For example, cadmium has been found to biologically mimic the substrate binding of zinc (Kamizono *et al.*, 1989). This is in part why Cd is toxic because although it can replace $Zn^{2+}$ structurally, it cannot replace it functionally (Hartwig, 2001). Likewise, dietary or genetic disruption of metal ion homeostasis, particularly copper and iron, causes many disease states (Fahrni, 2007, Madsen & Gitlin, 2007).

Homeostatic mechanisms governing the metallome are interconnected and a change in one regulatory process can impact others (Arino *et al.*, 2010, Bertinato & L'Abbe, 2004, Chillappagari *et al.*, 2010, Dann *et al.*, 2007, Dlouhy & Outten, 2013, Eide, 2009, Zhao *et al.*, 1998). For example, increases in intracellular Zn in *S. cerevisiae* have been attributed to increased expression of Fet4, which transports Cu, Fe, and Zn (Li & Kaplan, 1998, Pagani *et al.*, 2007). As such, characterization of the complete "metallome" is very important.

Finally, dynamic regulatory processes involved in homeostasis can lead to significant heterogeneity in elemental concentrations across a population of cells (Davey & Kell, 1996, Kalisky & Quake, 2011, Musat *et al.*, 2008, Leslie, 2011, Eide, 2009, Brehm-Stecher & Johnson, 2004). For all these reasons, a complete characterization of metal homeostasis requires not only the mean concentration of an element for a sample, but also the cell-to-cell variability in concentrations in order to truly understand homeostatic responses of the metallome. As such, there is a pressing need for high through-put techniques capable of elemental analysis of single cells.

There are several methods that have sufficient sensitivity to give single cell elemental compositions. These include mass spectrometry (MS), metal specific organic fluorophores, and intrinsic (x-ray) fluorescence (McRae et al., 2009, Penner-Hahn, 2014). Fluorescent probes have been used to report on subcellular transition metal cations such as Zn (Kikuchi et al., 2004) or Cu (Yang et al., 2005) and can have excellent sensitivity. However, these are generally less useful for paramagnetic ions, and even for diamagnetic metals, fluorescent probes are limited to detecting only the chelatable metal in the cell. Additionally, there is the potential of fluorophores to cause changes in metal composition. Mass spectrometric methods can have exquisite sensitivity and multielement detection capability. However, MS methods can suffer from matrix effects and haven't been widely used for single cell studies. There has been recent work using inductively coupled mass spectrometry (ICP-MS) for multiparametric analysis and simultaneous detection of multiple proteins in acidified biological samples using metal-tagged La-based antibodies. However, such methods are based on the unique signatures of the La-based antibodies which act as a surrogate for the target molecule to which the La-

labelled antibody is bound; they do not actually detect the native elemental content of cells (Ornatsky *et al.*, 2010). In contrast, XRF is always detectable, has minimal matrix effects, detects both bound and free metal ions in the cell, and is readily detected for most biologically relevant metals.

With the development of intense, third generation synchrotron sources, XRF imaging of intact cells using either dried or cryogenically frozen samples has become a widely used technique. Recent work (Wang *et al.*, 2014) involved raster scanning air-dried cells in fly-scan mode and implemented unsupervised cell identification to separate cell types and quantify the elemental content of individual cells from XRF datasets. This work successfully identified hundreds of cells using imaging techniques. However, imaging techniques do not permit easy time-dependent manipulations of cells, and aren't readily accessible to other techniques (e.g., light scattering, fluorescence cell sorting) which have been optimized for intact fluid cells. This paper describes the development and testing of an XRF-based flow cytometer that permits detection of total trace element levels in aquated, living cells, actively respiring, at high throughput.

## 2. Design

Our design goal for the XRF flow cytometer was ~ 1Hz cell sampling. This relatively slow rate is a result of the need to acquire appropriate counting statistics. At this rate, the jet flow and hydrodynamic focusing used in conventional cytometers are not possible. We have therefore fashioned a device that uses capillaries for loading and flowing cell samples with independent methodologies developed for hydrophilic and hydrophobic capillary materials.

The instrument includes two cameras to allow determination of cell position, and two fluorescence detectors. Each detector has been equipped with a Mo collimator to decrease detected scatter (Behne *et al.*, 2001). The distance between each detector is 2.8 cm giving a clearance for the sample holder of 1.4 cm and a sample-to-detector distance of 7 mm. For tests with hydrophilic capillaries, the sample-to-detector was ~2.5 cm. The sample holder is separate from the microscopes and detectors as shown in Figure 1.

For hydrophilic capillaries, the cell samples were contained in acrylic (PMMA - polymethylmethacrylate) capillaries (50 µm i.d., 100 µm o.d.) and were loaded using capillary action. The linear velocity while filling the capillary was ~1 mm $s^{-1}$ so that a 20 cm capillary takes ~10 minutes to fill. A water droplet was used to trap an air pocket at the end of the capillary in order to slow the cellular velocity from ~500 µm $s^{-1}$ to ~5 µm $s^{-1}$.

For hydrophobic capillaries, cells are loaded via syphon and we can accurately control velocity, with each 1 µm difference in height giving an increase in linear velocity of ~0.3 µm/s (25 µm id) or ~1.4 µm/s (50 µm id). In place of capillary action, a syringe was used to initially load the cells and establish a syphon pump for final control of cellular velocity. The syphon pump allows precise control of cell velocity as shown in Figure S1. As expected, velocity increased with Δh, due to hydrostatic pressure. Since capillary resistance scales as the inverse of the square of the radius, a capillary with 25 μm inner diameter shows approximately a 4-fold decrease in velocity compared to a 50 μm inner diameter.

Once the cells are loaded, the sample is aligned with the x-ray beam. The initial instrument was equipped with only a single microscope, and was thus insensitive to horizontal position. Since the beam is not horizontally uniform, a second microscope was added to the instrument to allow cells to be localized in the 2-dimensional plane along the horizontal profile of the beam. Combined with their vertical position from the images, this allowed for positioning of the cells in the 3D volume where the sample flow intersects the beam.

## 3. Conceptual Approach to Analysis

**Combining the XRF and video data sets -** Cells have variable sizes, metal content, velocities, and in some cases overlapping beam residence times, making single cell quantification of metal content impossible from the fitted XRF alone. In order to deconvolve the signals from cells one needs to know the path of each cell through the beam at every point in time when it is in the beam. Importantly, without visualizing capillary flow, it is impossible to know whether a peak in the XRF corresponds to a single cell or multiple overlapping cells (Crawford, 2015). Therefore, the cells, and the capillaries through which they flowed, were imaged with video data collected synchronously with XRF, using a horizontal visible-light microscope, (Mitutoyo, M Plan Apo 5x / 10 x objective; Infinitube Standard with Iris diaphragm; Edmund Optics 5012C, Color GigE Camera). Although the identification and tracking of objects in video data and the fitting of XRF data are well established techniques (Herrero & Bescós, 2009), we are not aware of previous efforts to combine XRF fitted time traces of elements with cellular "tracks" to deconvolve single cell total integrated fluorescence counts.

To align the video and XRF data, we first estimated the beam's location in the video. As the beam irradiates the capillary it also slowly (5-10 minutes) burns the capillary, discoloring it and providing a visual estimate of beam position.

To track the cells as they pass through the beam, each frame of the video was converted into a binary mask identifying the position and area of each cell in that frame. The x- and y-points were then connected across frames based on size and frame-to-frame mean-squared-displacement. The vertical profile of the beam was interpolated onto a grid, identical in size to the video frames, and aligned with the capillary beam image. Subsequent convolution of each cell's profile with the aligned grid, followed by column normalization to unity, gave an MxN array of theoretical fluorescence traces, where M is scan point (time) and N is cell number. This array is the predicted fluorescence for each cell as a function of time that would be detected if all cells had the same elemental mass, regardless of cell size, homogeneously distributed throughout the cell. Interpolation of the array's time frame onto the time frame of the XRF data and deconvolution of the amplitudes for each column allows the total integrated counts of each cell to be calculated using the entirety of the dataset.

Solving for coefficients, c, in the linear equation $Ac = F$ (where F is the XRF time trace for a given element, and A is the MxN array above) and then multiplying each column of the array A by the corresponding coefficient yields the fitted array of size MxN. Summation along each row of the fitted array gives the fitted elemental trace signal for a given time point. Summation down each column of this array gives the total detected counts for each cell, which is not proportional to concentration, due to the possibility of cells having variable residence time in the beam. Because each column of the initial array was normalized to unity, the coefficient c gives the elemental composition.

The values of the array are dependent on the alignment of the XRF and video data. This alignment is determined by the slope (differences in frame rate) and the intercept (differences in $t_0$) used to align the video and XRF time frames, as well as the alignment of the grid (its vertical shift and angle of rotation between the apparent normal vector of the video grid and the true normal vector associated with the profile). The slope, intercept, vertical shift and rotation angle were refined iteratively by testing combinations around the initial guess and minimizing the mean-squared-difference between the fitted array and the raw elemental trace of the element with the greatest signal to background ratio.

**Converting Counts to Mass –** Equation 1 was used to convert the total integrated counts to mass. The total fitted counts for each element depend on cell velocity and path-length (beam height). Assuming a constant Δy displacement from one time point to the next (i.e., assuming constant velocity), equation 1 gives the total mass of each element in each cell,

$$\boldsymbol{Cell\ Mass\ (fg)} = \frac{\mathbf{c \times v \times t}}{\boldsymbol{m \times h}} \qquad \mathbf{(1)}$$

where $\boldsymbol{c}$ is total fitted signal in units of counts $s^{-1}$ $I_0^{-1}$, $\boldsymbol{v}$ is the mean vertical rate of displacement of the cell in units of μm $s^{-1}$, $\boldsymbol{t}$ is the time the cell spends in the beam in units of s, $\boldsymbol{m}$ is the calibration slope in units of counts $s^{-1}$ $fg^{-1}$ $I_0^{-1}$, and $\boldsymbol{h}$ is the height of the beam in units of μm $s^{-1}$.

### 3.1. Integrating with respect to position

Since cell paths are non-uniform, cells need not have constant velocities. At each centroid position (x, y) the cell will give a ccertain number of integrated counts. To convert from the time domain to the space domain, first the y-points are sorted in increasing order. Then the corresponding x-points and integrated photon counts are reorganized to match the resorting of the y-points. These points are then used to interpolate integrated photon counts that would be associated with every integer y-position (pixel) of the cell through the beam. The area under this new curve is equivalent to the total integrated counts corresponding to the convolution of the beam given a per-scan cell vertical displacement equivalent to the pixel resolution of the camera divided by the objective magnification. This convolution is equivalent to the convolution seen for a cell traveling at a constant velocity of one pixel (distance) per unit scan (time). For example, XRF-flow cytometry data collected at 4 Hz synchronously with video data captured using a camera with a pixel resolution of 2.2 μm pixel$^{-1}$ equipped with a 5X objective (*i.e.*, a pixel separation of 0.44 microns pixel$^{-1}$) gives an apparent velocity associated with the new curve of 1.76 μm sec$^{-1}$.

## 4. Experimental

### 4.1.1. Sample Preparation and Handling

Trypsinized bovine red blood cells (bRBCs, 0.1 hematocrit, obtained from Lampire) were diluted 1:20-30 using phosphate buffered saline (PBS, Fisher Scientific) depending on capillary size. The stock and the diluted aliquots were kept at 4˚C. NIH3T3 cells were grown from cryopreserved aliquots in atmospheric $O_2$ and 5% $CO_2$ at 37°C. Cells were thawed and placed in 12 ml of complete medium (CM) [Dulbecco's modified Eagle medium, high glucose variant (4.5 mg ml$^{-1}$), supplemented with 10% donor bovine serum] in 75 cm$^2$ flasks at 5x10$^5$ cells flask$^{-1}$ (6.7 x 10$^3$ cells cm$^{-2}$). The cells were fed on day 2 (75% replacement) and then subcultured on day 5 into six 75 cm$^2$ flasks at 5.5x10$^5$ cells flask$^{-1}$. After 2 days of further proliferation, the cells were subcultured into twelve 75 cm$^2$ flasks at 5.5x10$^5$ cells flask$^{-1}$. The next day CM medium in flasks was increased from 12 ml to 200 ml. This CM medium increase promotes cell survival outside incubator at room temperature and atmospheric $CO_2$ levels for about a week. Cells were transported to APS and kept at room temperature and atmospheric $CO_2$ for 3-5 days. Cells were then harvested and resuspended in PBS solution for measurement of metal concentration. Yeast experiments were performed using the *Saccharomyces cerevisiae* yeast strain BY4741, grown in YPD rich media at 30 C˚ overnight. Cells were transported to APS in YPD media, stored at 4 C˚ and washed with PBS prior to measurement.

### 4.1.2. Sample Analysis

Experiments were performed using the Bio-CAT (Sector 18) and 20-ID-B beamlines available at the Advanced Photon Source at Argonne National Laboratories, Lemont, Illinois, USA. Data were measured using capillaries with i.d. 50 μm and o.d. 100 μm (hydrophilic capillaries - PMMA) and capillaries with i.d. 25 μm and o.d. 50 μm (hydrophobic capillaries – Zeonor®). Each position of the capillary was scanned for 5-10 minutes, while the XRF signal was captured at 4 Hz. Using an energy resolved solid state detector (Vortex-ME4, SII NanoTechnology), a typical scan detected between 20 – 60 cells depending on the cell density. After each scan, the capillary was translated by 100 μm vertically to avoid excessive radiation damage to the capillary.

The incident beam energy was selected using a Si(111) monochromator and gave a total incident flux of ~10$^{12}$ photons s$^{-1}$. Beam focusing was performed using a pair of Kirkpatrick-Baez mirrors, with the precise beam profile determined by a knife edge scan. For hydrophilic capillaries, the x-ray beam was focused to 50 µm horizontal x 20 µm vertical (FWHM). Due to the decreased size of hydrophobic capillaries, the x-ray beam was focused 25 µm horizontal x 6 µm vertical. Fluorescence counts were normalized to the incident intensity measured with a $N_2$ filled ion chamber immediately upstream from the sample.

XRF data were fit using the M-BLANK program (Crawford *et al.*, 2015). A blank was calculated using data from time points at which no cells were present in the beam, and was then subtracted from the data. The blank subtracted XRF for each time point was then fit in a linear least squares sense using a series of Gaussians with the energy calibration, Gaussian widths, and $K_\alpha$:$K_\beta$ ratios fixed at the experimentally determined or referenced values.

### 4.2. Instrument Calibration

The instrument was calibrated using standard solutions (~100, ~200, and ~500 µM $Cr(NO_3)_3$, $Fe(NO_3)_3$, $Ni(NO_3)_2$ in water) with concentrations confirmed by ICP-OES (Perkin-Elmer Optima 2000 DV with Winlab software) pre- and post-experiment. Due to lack of a calibration and the need to extrapolate, reported values for K are only semi-quantitative.

Prior to collecting XRF data for each standard, a blank scan of each capillary was obtained. The standard solutions were then loaded into capillaries via capillary action and the XRF spectra then obtained. Each blank was then subtracted from its associated XRF spectra and the blank-subtracted data was then fitted with a series of Gaussians, one for each Kα and Kβ peak; the summation of the area under the Kα and Kβ curves was taken as the fluorescence counts for each element. Instrument sensitivity (counts $fg^{-1}$ $s^{-1}$ $I_0^{-1}$) for each element was determined from the slope of the calibration curves and as expected, increased with increasing atomic number. The optimized parameters, energy calibration, Gaussian widths, and Kα:Kβ branching ratios from the standards were held constant in subsequent linear least-squares fits of the XRF data for the cytometer traces.

### 5. Results:

**Using hydrophilic capillaries of PMMA**, a total of 805 bRBC cells were detected in 24 individual scans taken over a time period of ~5 hours. The linear velocity (3.2 µm/sec ± 2.5 µm/sec) resulted in cells being exposed to the beam for a mean of ~5 seconds. A total of 31 mouse fibroblasts (NIH3T3) cells were detected in 6 individual scans taken over a time period of ~4 hours. The linear velocity (8.3 µm/sec ± 5.4 µm/sec) resulted in cells being exposed to the beam for a mean time of ~5.5 seconds.

From these measurements, a single bRBC gave a detectable Fe peak representing 58 ± 27 fg Fe $cell^{-1}$; no Zn peak above the noise level was detected in scans of single cells. For simple 3T3 cells the Zn and K fluorescence peaks are both above background noise; however, Fe is undetectable. The measured masses for Zn and K were 27 ± 16 fg cell$^{-1}$ and 789 ± 550 fg cell$^{-1}$, respectively. The histograms summarizing the Fe in bRBCs, the Zn and K in fibroblasts, and the correlation plot summarizing the relationship between Zn and K in fibroblasts are shown in Figure S2.

**Using hydrophobic capillaries of Zeonor®**, we were able to see signals from individual cells. Figure 2 shows fitted time course XRF spectra for Fe in bRBCs as well as K and Zn in yeast obtained using the hydrophobic Zeonor® capillaries with a 25 μm i.d. Twelve scans, each of 5 minutes, were made on bRBC samples detecting a total of 131 bRBCs. The measured masses for Fe, K, and Zn were 49.8 ± 29.7 fg cell$^{-1}$, slightly lower than the data collected using hydrophilic capillaries, 15.7 ± 14.7 fg cell$^{-1}$, and 0.37 ± 0.3 fg cell$^{-1}$, respectively. At the highest cell densities, we were able to interrogate 73 cells in a single 10 minute scan.

**Capillary Contaminants -** All of the capillaries that we tested showed non-negligible levels of Fe, K, Zn, and Cu contaminants with hydrophobic capillaries of Zeonor® and Zeonex® containing the lowest levels. To decrease contamination, we explored a variety of capillary materials (see Figure S3) and ultimately switched to Zeonor® due to relatively lower levels of contaminants.

This difference in the level of background caused by the contaminants in the capillaries matters in terms of detection limits and sensitivity. As can be seen in Figure 3, a comparison between the average bRBC XRF measured from 805 cells using hydrophilic capillaries and 73 cells using hydrophobic capillaries shows that even with far fewer cells, the data are much better with the smaller hydrophobic capillaries.

**Tests for Accuracy -** To test the accuracy of our data analyses, we examined the effect of background contamination, cell velocity, the horizontal variability of the beam, and cell density on the apparent Fe content.

*Background Fe Contamination* - Each position of each capillary (i.e., each individual scan containing multiple cells) was analyzed separately because of spatial differences in background contaminants. In order to test whether these variations in background interfered with cellular quantitation, we compared the apparent mean Fe content (from ~ 20 to 60 cells) from 24 different bRBC scans with their associated background level of Fe (see Figure S4). Despite a 50-fold variation in Fe background levels, the slope of the best fit line to the plot for signal vs. background (0.024 ± 0.050; 95% certainty interval; $r^2$-value, 0.053) is not distinguishable from zero, indicating that the background had no effect on Fe quantitation. Both the lowest and highest mean Fe masses are found for scans having among the lowest contamination. The population width may increase slightly for higher background levels, perhaps as a consequence of the larger uncertainty for a larger background.

*Cell Velocity and Mass Quantitation* - Depending on the details of capillary conditions there was a ~10-fold variation in cell velocity during measurement. If not properly accounted for in our analysis, this could affect the apparent XRF-determined masses. A plot of calculated Fe content as a function of cellular velocity through the beam shows no dependence of the apparent Fe content on cell velocity (see Figure **S5**).

*The influence of the horizontal profile* of the beam on the observed distribution of Fe masses in bRBCs is shown in Figure 4, where the apparent Fe content is plotted as a function of the x-coordinate of each cell. The experimentally determined horizontal beam profile is overlaid on this plot. There is a weak dependence of quantitation on the horizontal position, most likely reflecting intensity variations along the horizontal profile of the beam. To correct for this, we calculated the least-squares fit of the horizontal profile of the Fe composition to the beam profile and used the fitted profile to correct the masses for their x-position (Figure 4B). Figure 4C and D show the histograms of the cellular Fe composition before and after correction by the horizontal profile.

*Cell Density* - For some scans, the cellular concentration was high enough that two or more cells were in the beam at the same time. In order to test whether we were able to reliably deconvolve these signals we compared the apparent distributions for overlapping vs. non-overlapping cells (see Figure **S6**). Based on data from the first instrument, using only one camera, both the mean Fe content and the apparent width of the distribution in metal content increase if more than two cells were in the beam at the same time (See Figure S6). This could be an inability of our fitting algorithm to reliably assign fluorescence to individual cells when more than two cells were in the beam. However, this could also reflect the impact of not being able to account for cellular position along the horizontal profile of the beam for this data set. The horizontal profile of the beam for this data set was noticeably skewed from a Gaussian distribution. In the absence of crowding (*i.e.*, overlapping residence times of greater than two cells) cells flowed roughly through the center of the capillary and therefore sampled primarily the central portion of the horizontal profile of the beam. Additionally, for that dataset, wider capillaries meant an increased FWHM for the horizontal profile and therefore a more gradual change in flux density per micron along the profile. However, increased cell density could push cells outside the center of the capillary and lead to cells sampling a broader range of flux densities causing the results seen here. Without a second microscope to correct for variable horizontal positioning due to crowding, it was impossible to address. However, given our results from the second instrument, this seems plausible. Accordingly, all of the analyses for this first data set exclude cases with more than two cells in the beam at any given time in order to avoid deviation of cell positioning from the center of the capillary.

## 6. Discussion:

Ultimately, single cell detectability is sufficient to give metal compositions for trace elements and we can see Fe and K in single bRBCs, Zn in single 3T3 cells, as well as K and Zn in single yeast cells (Figure 5). Our inability to see Zn (bRBC) or Fe (3T3 and yeast) is consistent with known concentrations in each case as these are below our current detection limits (~7fg for Fe, ~2.3 fg for Zn, and ~30 pg for K).

Even with these noisy data, we can see the importance of single-cell measurements. The distribution of Fe is much larger than expected from uncertainty. The experimentally determined mean Fe content for individual bRBCs, 58 fg (± 27 fg), is in good agreement with previous findings (Herring *et al.*, 1960a, Kakkar & Makkar, 2009, Shamberger, 2003). One of the striking observations for our data is the surprisingly wide distribution in metal masses, with a 1.9-fold difference between the cutoff for the lowest quartile (39.9) and the highest quartile (76.7). Given the relatively noisy signal (i.e., Figure 4) one might assume that the width of the distributions in Figure 5 is the result of noisy data. However, an average bRBC traveling at the average velocity, gives ~173 fluorescent counts and ~20 background counts for Fe during its residence time in the beam, corresponding to a statistical uncertainty of ~ $\frac{\sqrt{193}}{173}$ = 8.0 % or ~ 4.7 fg. The observed standard deviation (27 fg) is more than 6 times larger, suggesting that the distribution is dominated by biological variability not experimental uncertainty. In principle, variations in cell size might account for this. However, a plot of mass vs cell radius shows no apparent correlation (Figure 6) suggesting that this may be a biologically relevant distribution, perhaps reflecting different call age.

We were able to experimentally determine both Zn and K content of individual NIH3T3 mouse fibroblasts with Zn quantitation being in good agreement with known mammalian concentrations (Eide, 2006). These showed 2.3- and 2.8- fold differences between the 1st (16.3, 421) and 3rd (37.7, 1160) quartiles for Zn and K, respectively. Results for the measured distribution widths from NIH3T3 cells are similar to those from bRBCs above with experimental uncertainties of ±3 and ±53 fg for Zn and K, vs measured distribution widths of 16 and 550 fg, respectively. Note that although the relative K concentrations for different cells are valid, the lack of a calibration standard for K means that the K quantitation is only an estimate, based on extrapolating the instrumental sensitivity from higher-Z elements.

The switch to smaller capillaries gives a much better determination of the distribution of masses for each element. Importantly, based solely on counting statistics, the mean absolute error for K, S, Zn, and Fe are 1.0 fg, 3.3 fg, 0.38 fg, and 0.86 fg, respectively; this gives percent errors of 6.3% 14%, 10%, and 1.7%, respectively. This shows almost a 4.5-fold improvement in signal quality over the initial instrument designs. Importantly, our calculated Fe:Zn ratio for bRBCs matches literature values (Kakkar & Makkar, 2009, Herring *et al.*, 1960a, Herring *et al.*, 1960b, Wang *et al.*, 2014).

With two cameras we were able to demonstrate that the apparent Fe concentration is only moderately impacted by horizontal deviations of the capillaries/cells from the center of the profile. For a Gaussian distributed horizontal profile for the X-ray beam, this deviation appears to result in a somewhat lower apparent population mean and a greater percentage population distribution. This can be seen by comparing Figure 4C and D.

In addition to the data collected for the bRBCs and mouse fibroblasts, we've also been able to measure the elemental compositions of yeast. Although these data are less impressive, this is not surprising given the lower total content of metals in yeast. For example, two scans each of 5 minutes were made on yeast samples with different cell densities allowing us to interrogate 18 cells. These cells showed S, Zn, and K with mean content of 0.57 ± 0.61 fg, 0.62 ± 0.45 fg, and 37.1 ± 41.5 fg, respectively.

## 7. Conclusions:

The smaller capillaries (25 μm id, 50 μm od) allowed us to detect more elements. We have significantly improved the signal-to-noise ratio for Fe in bRBCs from 41 to 119 for a spectrum sum of all cells in a scan. Additionally, we are now able to see S, K, and Zn in bRBCs with associated signal-to-noise ratios of 3, 6.5, and 2, respectively. The agreement of both Fe and Zn with literature is very important as these elements were part of the calibration standards. In terms of yeast, when looking at the spectrum sum of all cells from a scan, we are able to see S, K, and Zn with a signal-to-noise ratio of 2, 10, and 5 respectively. The ability to see S here is impressive given background concentrations of Cl on the order of ~200mM. Unfortunately, at the level of an individual cell we were unable to see S. Addition of a He shroud to reduce background scatter should extend our detection limits ever further. Collectively, these results show promising potential for the future development of the cytometer to explore the cellular metallome.

**Acknowledgements** This research was funded by the National Science Foundation under grant number NSF-IDBR-0852802. This research used resources of the Advanced Photon Source, a U.S. Department of Energy (DOE) Office of Science User Facility operated for the DOE Office of Science by Argonne National Laboratory under Contract No. DE-AC02-06CH11357. "This project was supported by grant 9 P41 GM103622 from the National Institute of General Medical Sciences of the National Institutes of Health." The content is solely the responsibility of the authors and does not necessarily reflect the official views of the National Institute of General Medical Sciences or the National Institutes of Health. Sector 20 facilities at the Advanced Photon Source, and research at these facilities, are supported by the US Department of Energy - Basic Energy Sciences, the Canadian Light Source and its funding partners, the University of Washington, and the Advanced Photon Source. Use of the Advanced Photon Source, an Office of Science User Facility operated for the U.S. Department of Energy (DOE) Office of Science by Argonne National Laboratory, was supported by the U.S. DOE under Contract No. DE-AC02-06CH11357. The staff of the LSA Scientific Instruments Shop provided valuable collaboration on sample holder design. The authors would like to thank Erik Guetschow from the Kennedy Lab for his collaboration on a working syphon pump.

## References

Arino, J., Ramos, J. & Sychrova, H. (2010). *Microbiology and Molecular Biology Reviews* **74**, 95-120.

Behne, E. A., Feng, Y., Seidler & T., G. (2001). *Review of Scientific Intruments* **72**, 3908-3913.

Bertinato, J. & L'Abbe, M. R. (2004). *Journal of Nutritional Biochemistry* **15**, 316-322.

Brehm-Stecher, B. F. & Johnson, E. A. (2004). *Microbiology and Molecular Biology Reviews* **68**, 538-559.

Chillappagari, S., Seubert, A., Trip, H., Kuipers, O. P., Marahiel, M. A. & Miethke, M. (2010). *Journal of Bacteriology* **192**, 2512-2524.

Crawford, A. (2015). Ph.D. thesis, University of Michigan.

Crawford, A., Deb, A. & Penner-Hahn, J. (2015). M-BLANK: a set of software tools for the fitting of imaging and time course x-ray fluorescence data sets (to be published).

Dann, C. E., Wakeman, C. A., Sieling, C. L., Baker, S. C., Irnov, I. & Winkler, W. C. (2007). *Cell* **130**, 878-892.

Davey, H. M. & Kell, D. B. (1996). *Microbiological Reviews* **60**, 641-696.

Dlouhy, A. C. & Outten, C. E. (2013). *Metallomics and the Cell*, edited by L. Banci, pp. 241-278. Dordrecht: Springer.

Eide, D. J. (2006). *Biochimica Et Biophysica Acta-Molecular Cell Research* **1763**, 711-722.

Eide, D. J. (2009). *Journal of Biological Chemistry* **284**, 18565-18569.

Fahrni, C. J. (2007). *Current Opinion in Chemical Biology* **11**, 121-127.

Hartwig, A. (2001). *Antioxid. Redox Signal.* **3**, 626-634.

Herrero , S. & Bescós, J. (2009). *Background Subtraction Techniques: Systematic Evaluation and Comparative Analysis*. Verlag Berlin Heidelberg: Springer.

Herring, W. B., Leavell, B. S., Paixao, L. M. & Yoe, J. H. (1960a). *American Journal of Clinical Nutrition* **8**, 846-854.

Herring, W. B., Leavell, B. S., Paixao, L. M. & Yoe, J. H. (1960b). *American Journal of Clinical Nutrition* **8**, 855-863.

Kakkar, N. & Makkar, M. (2009). *Lab Medicine* **40**, 549-555.

Kalisky, T. & Quake, S. R. (2011). *Nature Methods* **8**, 311-314.

Kamizono, A., Nishizawa, M., Teranishi, Y., Murata, K. & Kimura, A. (1989). *Molecular & General Genetics* **219**, 161-167.

Kikuchi, K., Komatsu, K. & Nagano, T. (2004). *Current Opinion in Chemical Biology* **8**, 182-191.

Leslie, M. (2011). The Power Of One, Vol. 331, Science, pp. 24-26.

Li, L. T. & Kaplan, J. (1998). *Journal of Biological Chemistry* **273**, 22181-22187.

Madsen, E. & Gitlin, J. D. (2007). *Annual Review of Neuroscienc* **30**, 317-337.

McRae, R., Bagchi, P., Sumalekshmy, S. & Fahrni, C. J. (2009). *Chemical Reviews* **109**, 4780-4827.

Musat, N., Halm, H., Winterholler, B., Hoppe, P., Peduzzi, S., Hillion, F., Horreard, F., Amann, R., Jorgensen, B. B. & Kuypers, M. M. M. (2008). *Proceedings of the National Academy of Sciences of the United States of America* **105**, 17861-17866.

Ornatsky, O., Bandura, D., Baranov, V., Nitz, M., Winnik, M. A. & Tanner, S. (2010). *Journal of Immunological Methods* **361**, 1-20.

Pagani, M. A., Casamayor, A., Serrano, R., Atrian, S. & Arino, J. (2007). *Molecular Microbiology* **65**, 521-537.

Penner-Hahn, J. E. (2014). *Metallomics and the Cell*, edited by L. Banci. Dordrecht: Springer.

Shamberger, R. J. (2003). *Biological Trace Element Research* **94**, 123-129.

Vogt, S. (2003). *J. Phys. IV France* **104**, 635-638.

Wang, S. W., Ward, J., Leyffer, S., Wild, S. M., Jacobsen, C. & Vogt, S. (2014). *Journal of Synchrotron Radiation* **21**, 568-579.

Yang, L. C., McRae, R., Henary, M. M., Patel, R., Lai, B., Vogt, S. & Fahrni, C. J. (2005). *Proc. Natl. Acad. Sci.* **102**, 11179-11184.

Zhao, H., Butler, E., Rodgers, J., Spizzo, T., Duesterhoeft, S. & Eide, D. (1998). *Journal of Biological Chemistry* **273**, 28713-28720.

**Figure 1** Instrument Design: An eagle-eye's view of the instrument, i.e., the two horizontal microscopes, sample holder and detectors.

**Figure 2** Time Scans: Representative time-scans for Fe channel for bRBC (top) and Zn and K channels for yeast (bottom). The y-axis is in units of counts $s^{-1}$ $usic^{-1}$ normalized to an absolute intensity of 1. For yeast, Zn has been vertically shifted for visualization.

**Figure 3** Mean Integrated Spectra: The mean integrated XRF Spectrum for 805 bRBC with hydrophilic capillary (top), 78 bRBCs with hydrophobic capillary (middle), and 18 yeast (bottom).

**Figure 4** Correcting Fe Masses by the Horizontal Profile of the Beam: A Levenburg-Marquadt algorithm to optimize three variables of the beam profile: the amplitude, intercept and horizontal shifting. I think this looks really good. The final distribution looks like the distributions from the first manuscript (albeit, the mean is slightly higher).

**Figure 5** Single Cell Spectra: XRF data for single cells of bRBC (top-left), yeast (top-right), and 3T3 (bottom). The 3T3 data were measured with a 50 µm i.d. hydrophilic capillary and thus have worse S/N in comparison with the other data (measured using 25 µm i.d. hydrophobic capillaries).

**Figure 6** Cell Radii vs Mass: The apparent mass of each cell from a single scan of bRBCs were plotted against the radius as measured in video pixels.

**Figure 1**

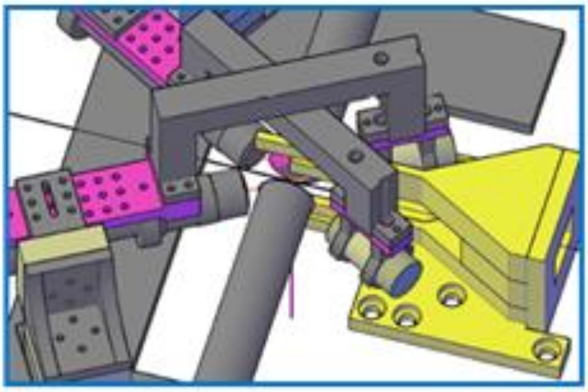

**Figure 2**

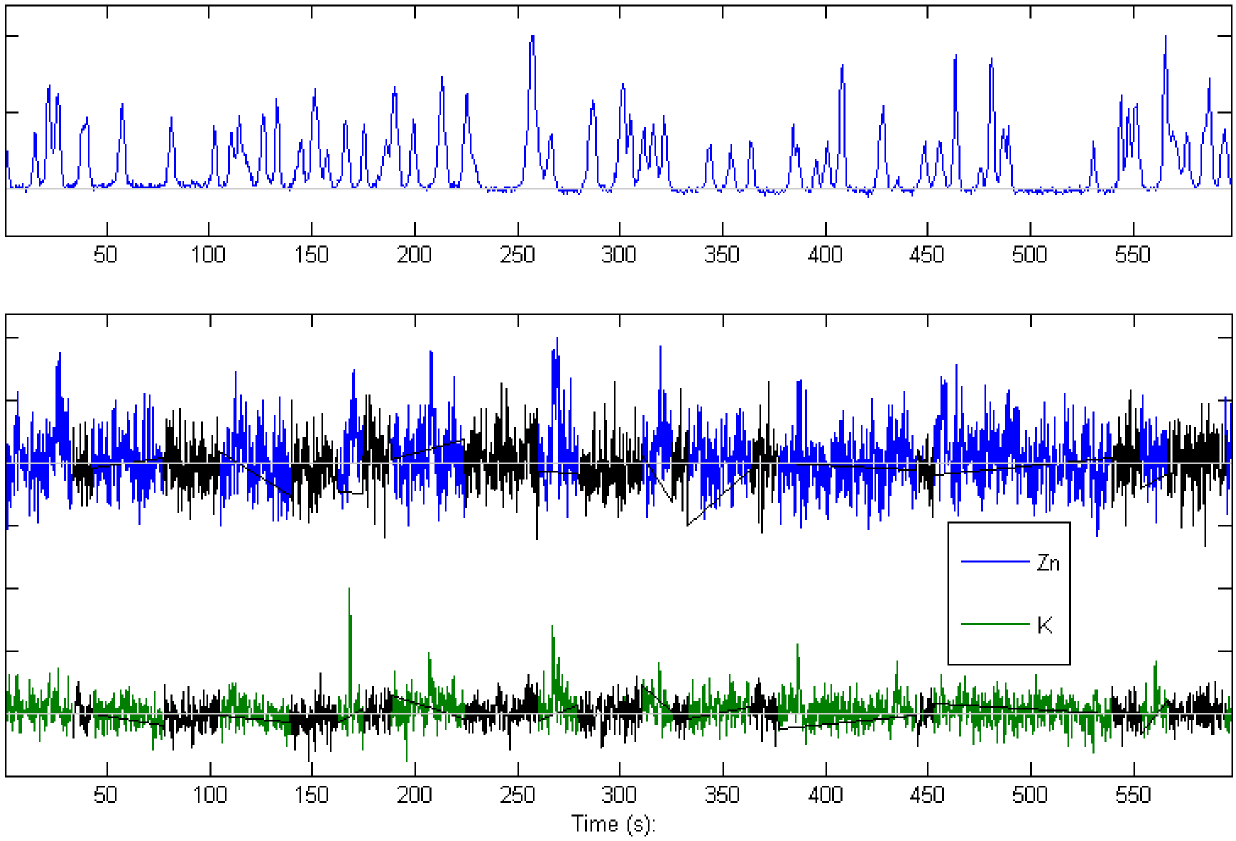

**Figure 3**

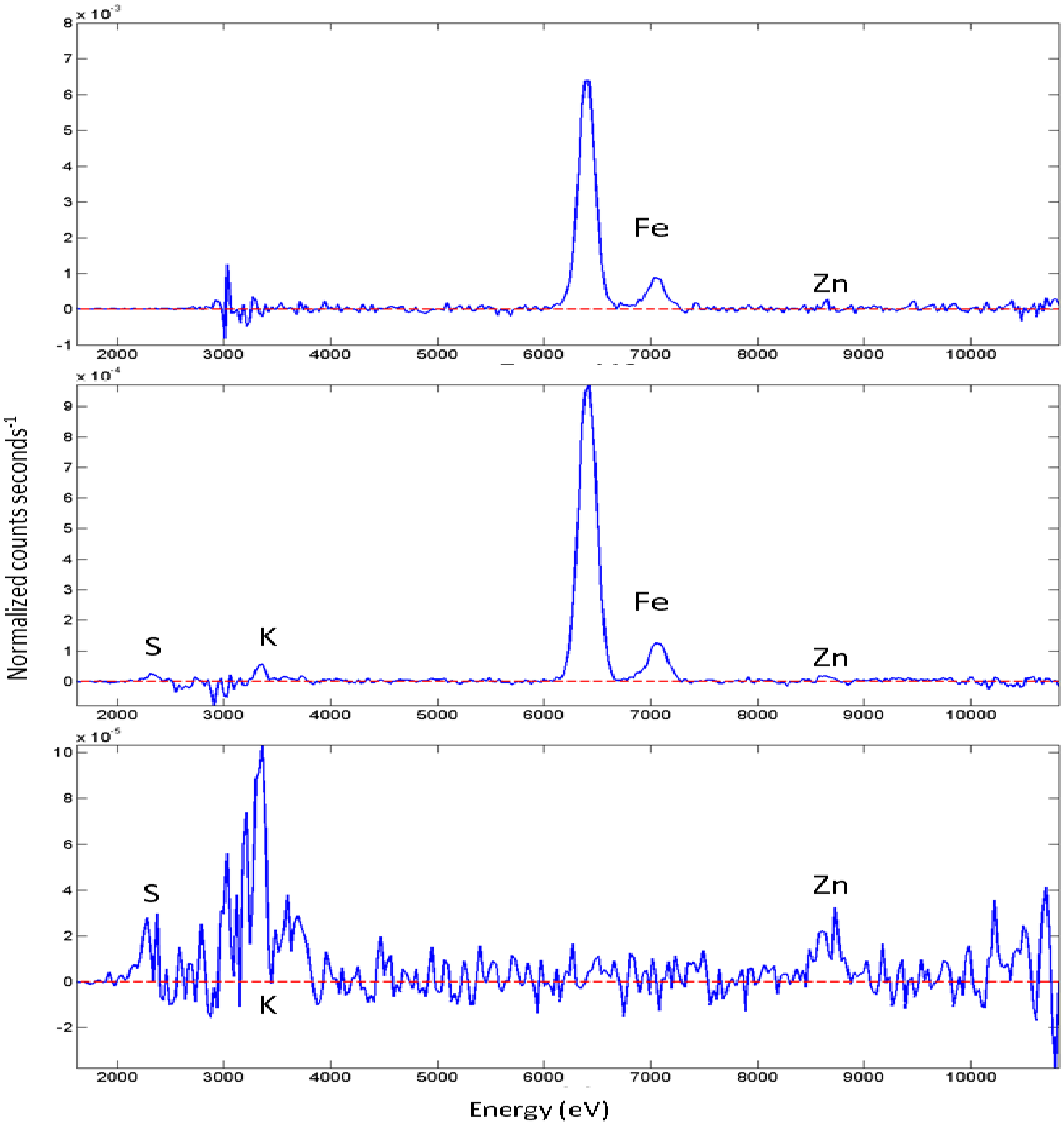
x 10^-3
8
7
6
5
4
3
2
1
0
-1
Fe
Zn
2000
3000
4000
5000
6000
7000
8000
9000
10000
x 10^-4
9
8
7
6
5
4
3
2
1
0
S
K
Fe
Zn
x 10^-5
10
8
6
4
2
0
-2
S
K
Zn
Normalized counts seconds-1
Energy (eV)

**Figure 4**

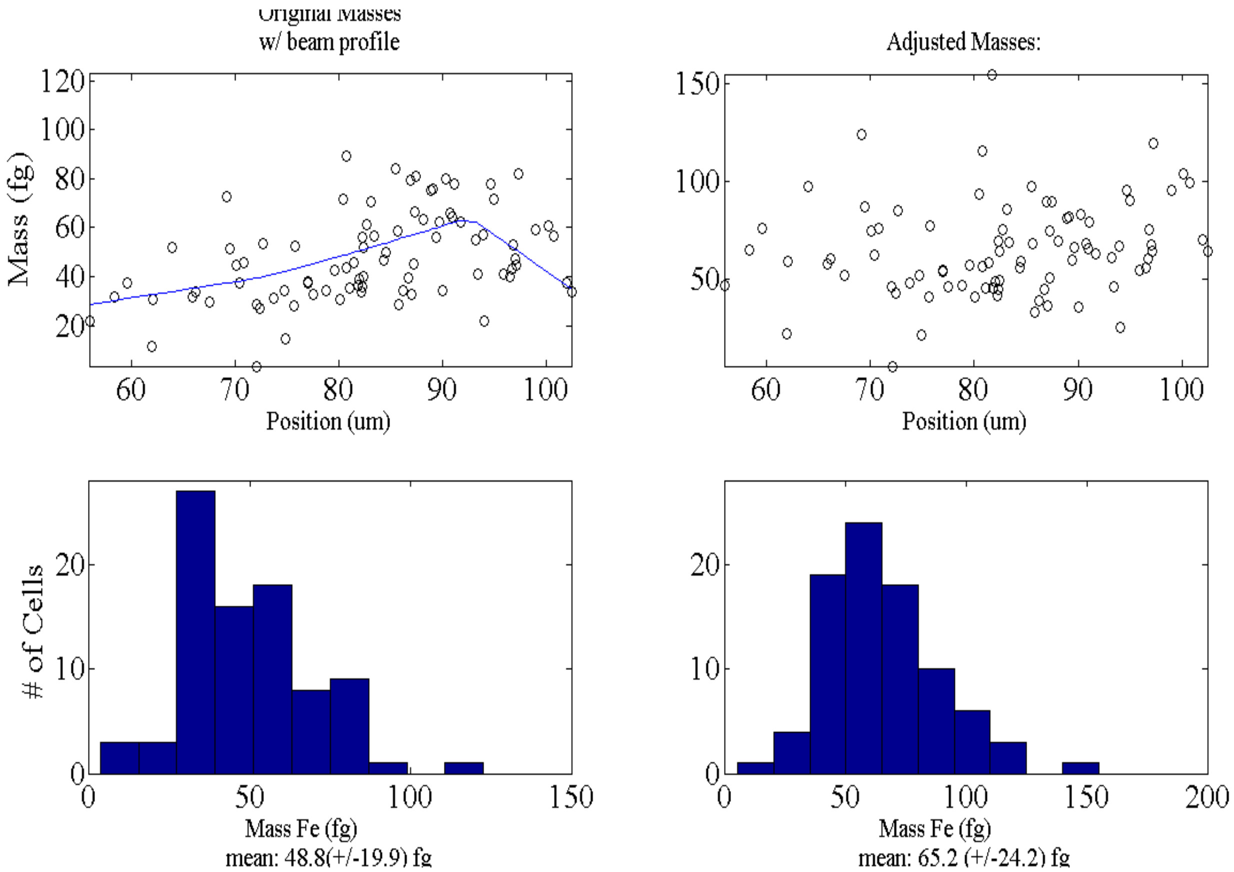
Original Masses
w/ beam profile
Adjusted Masses:
Mass (fg)
120
100
80
60
40
20
150
100
50
60
70
80
90
100
Position (um)
Position (um)
# of Cells
20
10
0
0
50
100
150
200
Mass Fe (fg)
mean: 48.8(+/-19.9) fg
Mass Fe (fg)
mean: 65.2 (+/-24.2) fg

**Figure 5**

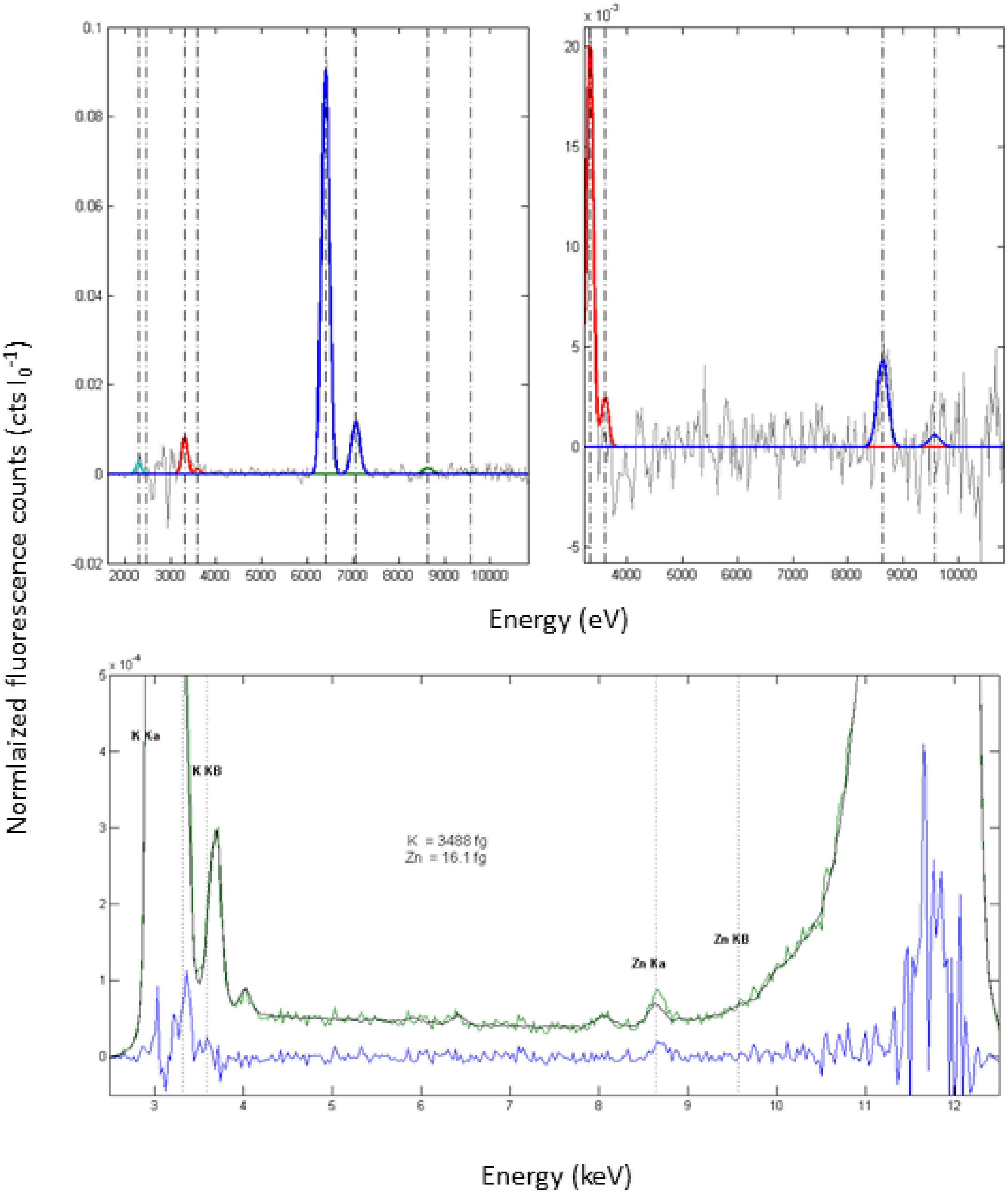
Normlaized fluorescence counts (cts $I_0^{-1}$)
0.1
0.08
0.06
0.04
0.02
0
-0.02
2000
3000
4000
5000
6000
7000
8000
9000
10000
x 10⁻³
20
15
10
5
0
-5
4000
5000
6000
7000
8000
9000
10000
Energy (eV)
x 10⁻⁴
5
4
3
2
1
0
K Ka
K KB
K = 3488 fg
Zn = 16.1 fg
Zn Ka
Zn KB
3
4
5
6
7
8
9
10
11
12
Energy (keV)

# Figure 6

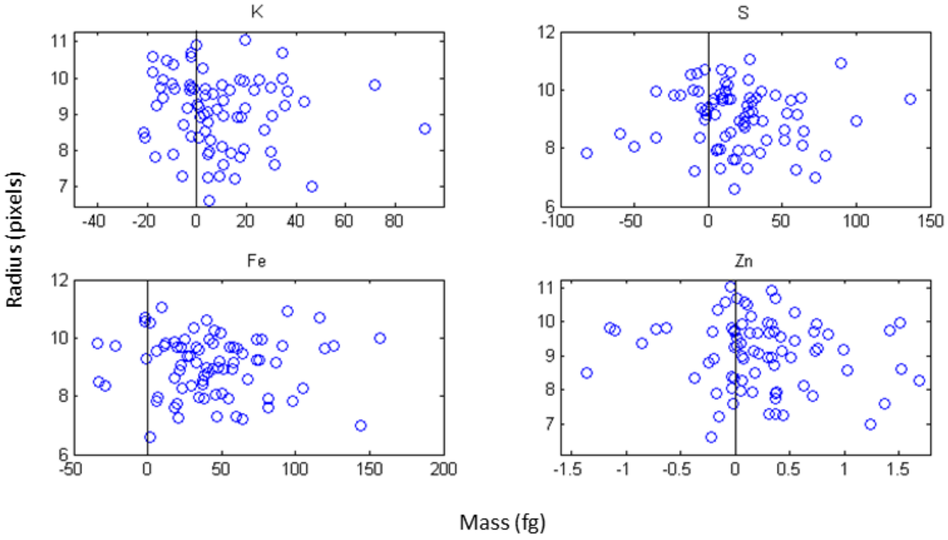
K
S
Fe
Zn
Radius (pixels)
Mass (fg)
11
10
9
8
7
-40
-20
0
20
40
60
80
12
10
8
6
-100
-50
0
50
100
150
12
10
8
6
-50
0
50
100
150
200
11
10
9
8
7
-1.5
-1
-0.5
0
0.5
1
1.5

# Supporting information

**Figure S1** Syphon Pump Tests: The plots of cellular velocities of two different capillaries as a function of the relative height difference of the two sample holders of the syphon pump. PMMA, polymethylmethacrylate; Znr, Zeonor®; the trailing numbers refer to the inner and outer diameters of the capillary, respectively.

**Figure S2** Distributions and Correlations: (A) a cell-mass histogram for Fe in bovine bRBCs; (B) a cell-mass histogram of Zn in NIH3T3 mouse fibroblasts; (C) a cell-mass histogram for K in NIH3T3 mouse fibroblasts; and (D) a correlation plot of K vs. Zn for NIH3T3 mouse fibroblasts.

**Figure S3** XRF Spectra of Capillary Materials: An overlay of the XRF spectra, obtained for the different capillary materials, normalized to their associated baseline height between ~5200 eV and ~5500 eV. Legend definitions: PC – Polycabonate; PETG - Polyethylene Terephtalate Glycol-modified; PMMA – Polymethylmethacrylate; PP – Polypropylene; PS – Polystyrene; Zex – Zeonex; Zor – Zeonor.

**Figure S4** Mean Quantitation vs. Background Contamination: The effect of the background Fe contamination on the apparent bRBC Fe concentration. The mean (black) and std. deviation (red) of Fe concentration for each scan is plotted vs the background Fe contamination

**Figure S5** Velocity vs. bRBC Fe Content: Comparison of the mean cellular velocity of a particular cell during its residence time with its calculated Fe content. Expectedly, there is a slope of zero indicating no relation between the two variables.

**Figure S6** Overlapping residence versus the associated distribution width: Using a two tailed F-Test, with 80% certainty, we can state that the population distribution obtained from three cells sharing residence through the beam is statistically different from that obtained from two cells overlapping or that of lone cells.

**S1**

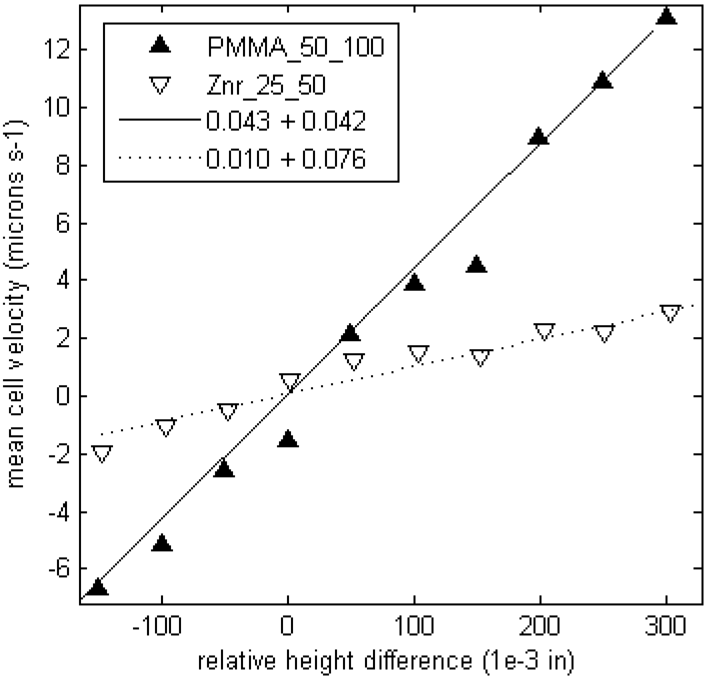
▲ PMMA_50_100
▽ Znr_25_50
0.043 + 0.042
0.010 + 0.076
mean cell velocity (microns s-1)
relative height difference (1e-3 in)
12
10
8
6
4
2
0
-2
-4
-6
-100
0
100
200
300

**S2**

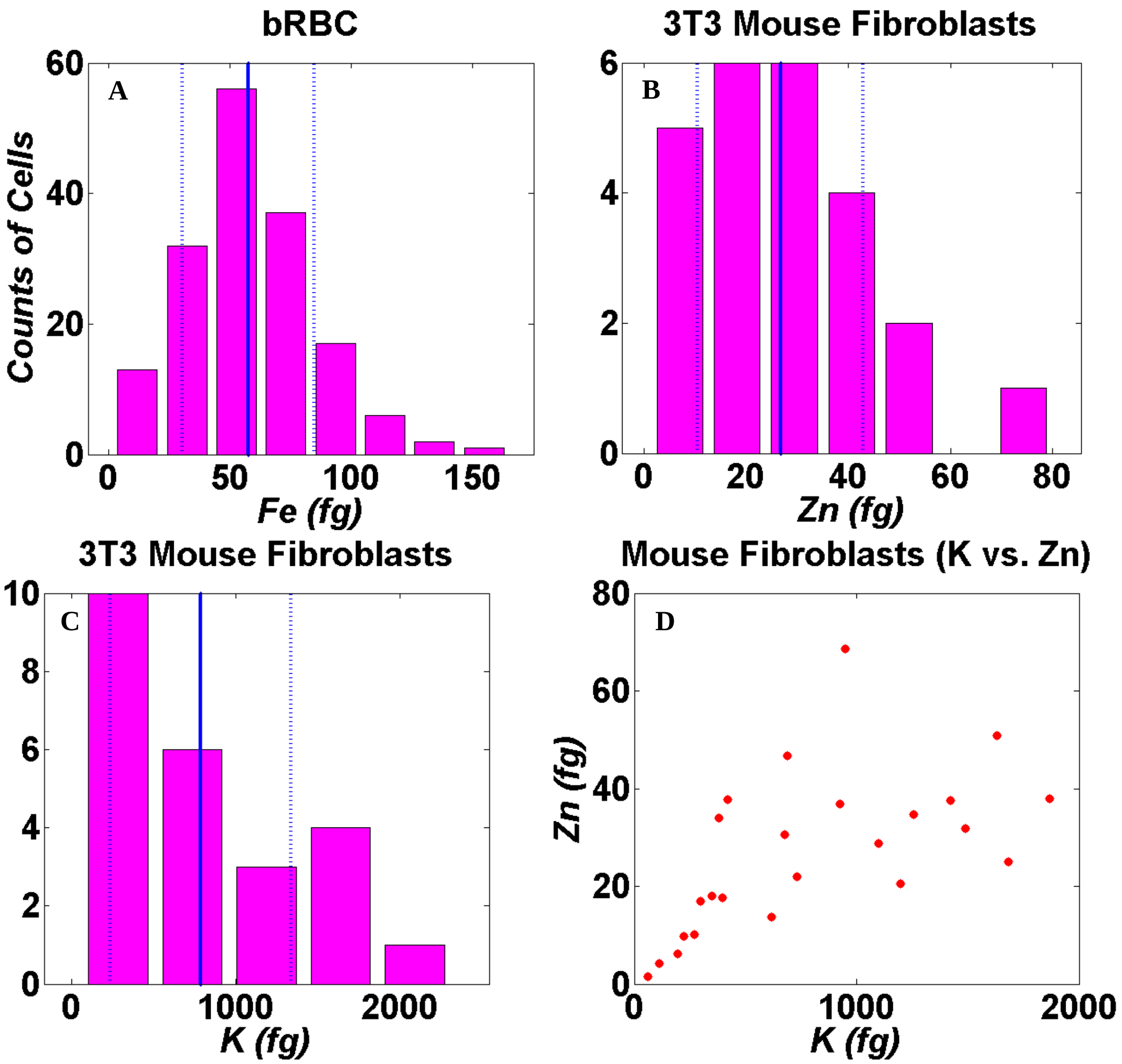
bRBC
A
Counts of Cells
60
40
20
0
0
50
100
150
Fe (fg)
3T3 Mouse Fibroblasts
B
6
4
2
0
0
20
40
60
80
Zn (fg)
3T3 Mouse Fibroblasts
C
10
8
6
4
2
0
0
1000
2000
K (fg)
Mouse Fibroblasts (K vs. Zn)
D
Zn (fg)
80
60
40
20
0
0
1000
2000
K (fg)

## S3

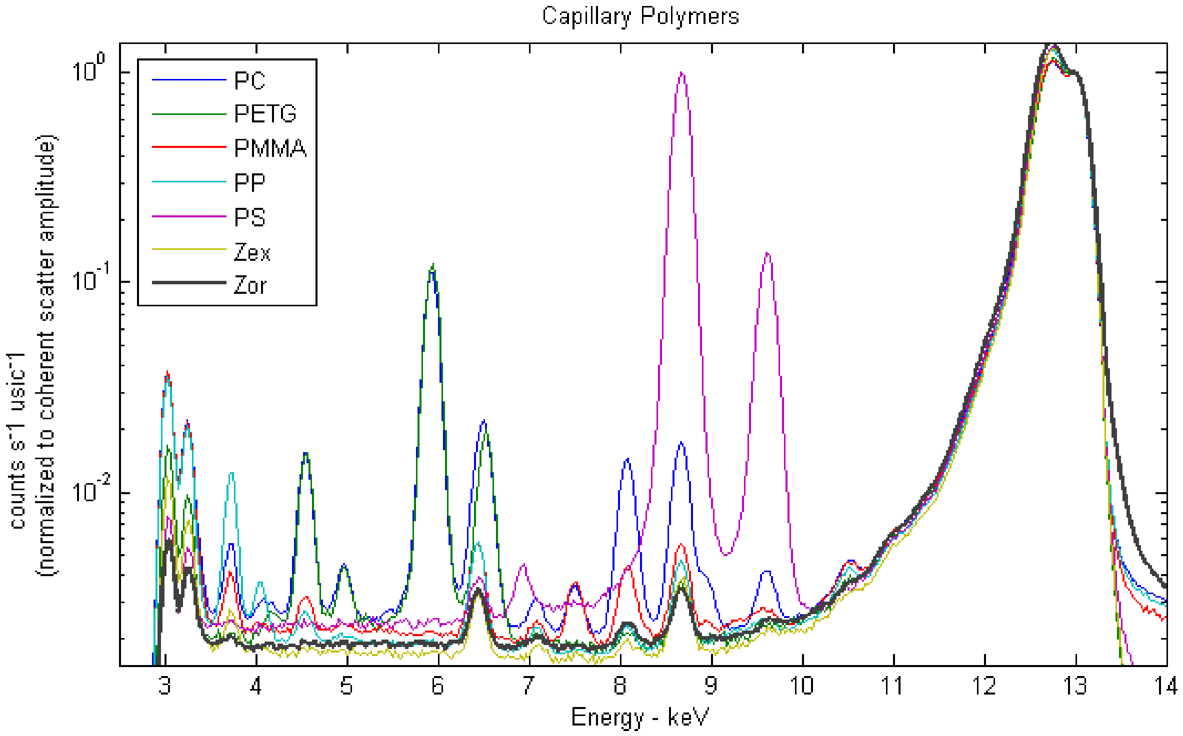
Capillary Polymers
PC
PETG
PMMA
PP
PS
Zex
Zor
$10^0$
$10^{-1}$
$10^{-2}$
counts s-1 usic-1
(normalized to coherent scatter amplitude)
3
4
5
6
7
8
9
10
11
12
13
14
Energy - keV

**S4**

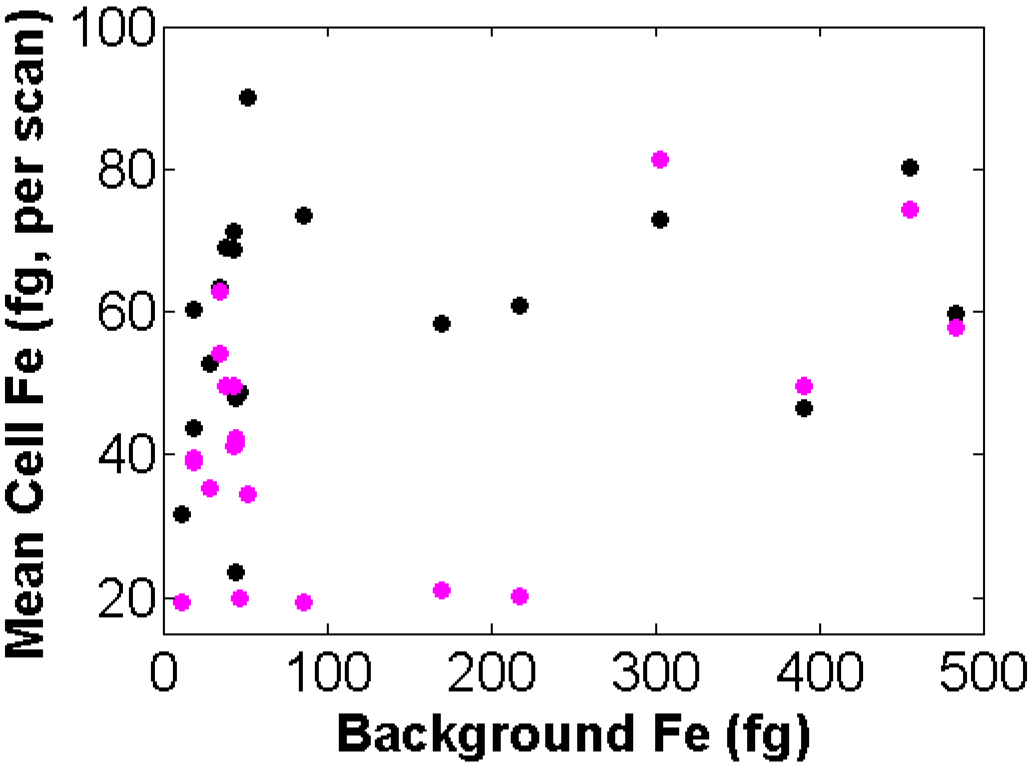
Mean Cell Fe (fg, per scan)
100
80
60
40
20
0
100
200
300
400
500
Background Fe (fg)

**S5**

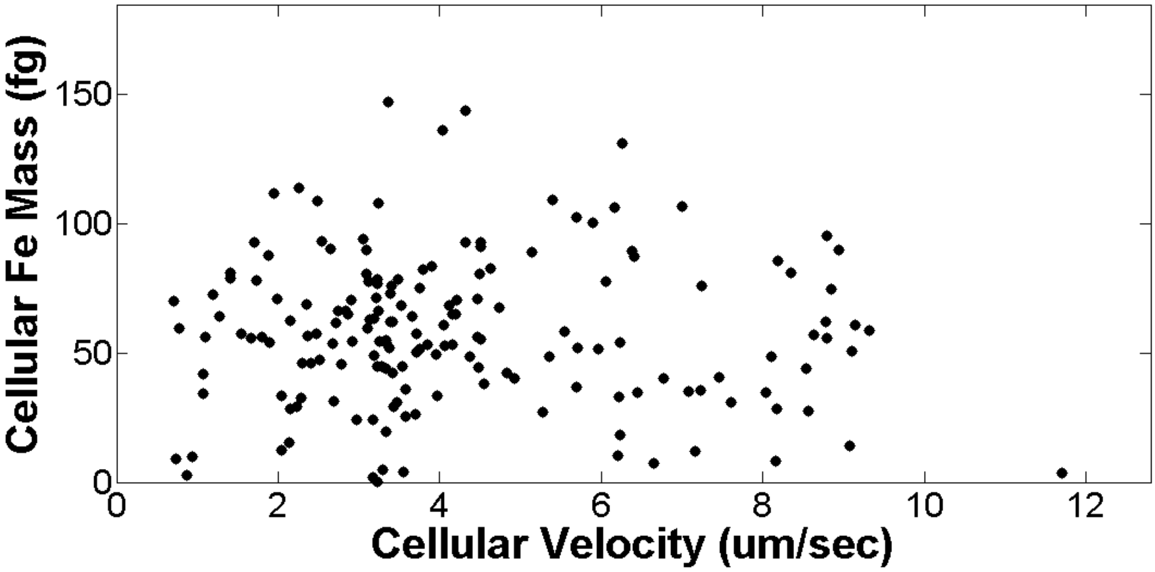
Cellular Fe Mass (fg)
0
50
100
150
Cellular Velocity (um/sec)
0
2
4
6
8
10
12

**S6**

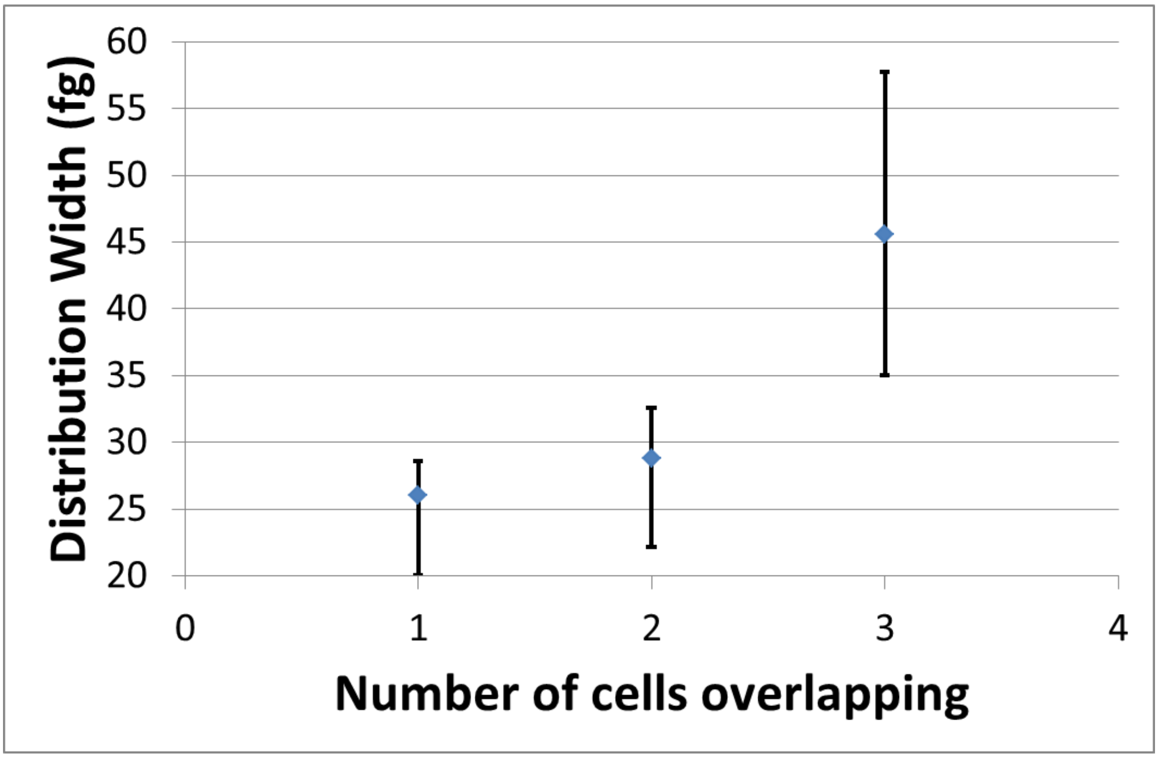
Distribution Width (fg)
60
55
50
45
40
35
30
25
20
0
1
2
3
4
Number of cells overlapping